

# 1 Global fine-mode aerosol radiative effect, as constrained by 2 comprehensive observations

3 Chul E. Chung<sup>1</sup>, Jung-Eun Chu<sup>2</sup>, Yunha Lee<sup>3</sup>, Twan van Noije<sup>4</sup>, Hwayoung Jeoung<sup>5</sup>, Kyung-Ja  
4 Ha<sup>2</sup>, Marguerite Marks<sup>6</sup>

5 <sup>1</sup>Desert Research Institute, Reno, 89512, USA

6 <sup>2</sup>Pusan National University, Busan, 46241, Korea

7 <sup>3</sup>Washington State University, Pullman, 99164, USA

8 <sup>4</sup>Royal Netherlands Meteorological Institute, AE De Bilt, 3730, Netherlands

9 <sup>5</sup>National Meteorological Satellite Center, 27803, Korea

10 <sup>6</sup>Carnegie Mellon University, Pittsburgh, 15213, USA

11 *Correspondence to:* C. E. Chung ([Eddy.Chung@dri.edu](mailto:Eddy.Chung@dri.edu))

12 **Abstract.** Aerosols directly affect the radiative balance of the Earth through absorption and scattering of solar  
13 radiation. Although the contributions of absorption (heating) and scattering (cooling) of sunlight have proved  
14 difficult to quantify, the consensus is that anthropogenic aerosols cool the climate, partially offsetting the warming  
15 by rising greenhouse gas concentrations. Recent estimates of global direct **anthropogenic** aerosol radiative forcing  
16 (i.e., global radiative forcing due to aerosol-radiation interactions) are  $-0.35 \pm 0.5 \text{ Wm}^{-2}$ , and these estimates depend  
17 heavily on aerosol simulation. Here, we integrate a comprehensive suite of satellite and ground-based observations  
18 to constrain total AOD, its fine-mode fraction, the vertical distribution of aerosols and clouds, and the co-location of  
19 clouds and overlying aerosols. We find that direct fine-mode aerosol radiative effect is  $-0.46 \text{ Wm}^{-2}$  ( $-0.54 \sim -0.39$   
20  $\text{Wm}^{-2}$ ). Fine-mode aerosols include sea salt and dust aerosols, and we find that these natural aerosols pose a very  
21 large cooling ( $-0.44 \sim -0.26 \text{ Wm}^{-2}$ ) when constrained by observations. When the contribution of these natural  
22 aerosols is subtracted from the fine-mode radiative effect, the net becomes  $-0.11$  ( $-0.28 \sim +0.05$ )  $\text{Wm}^{-2}$ . This net  
23 arises from total (natural + anthropogenic) carbonaceous, sulfate and nitrate aerosols, which suggests that global  
24 direct **anthropogenic** aerosol radiative forcing be less negative than  $-0.35 \text{ Wm}^{-2}$ .

## 25 1. Introduction

26 Atmospheric aerosols absorb and scatter solar radiation and act as cloud condensation nuclei, thus affecting  
27 cloud albedo and lifetime. The climatic effect of anthropogenic aerosols is usually quantified in terms of radiative  
28 forcing, defined as the net radiative flux perturbation at the top of the atmosphere (TOA) owing to aerosol changes  
29 since pre-industrial time to the present. The magnitude of aerosol radiative forcing is recognized as the most  
30 uncertain component of estimated total radiative forcing (Myhre et al., 2013a). The magnitude of the global average  
31 of aerosol direct radiative forcing (which is referred to as radiative forcing due to aerosol-radiation interactions in  
32 the 5<sup>th</sup> IPCC report) has been estimated to range from  $-0.85$  to  $+0.15 \text{ Wm}^{-2}$  (Myhre et al., 2013a).

33 Direct aerosol forcing has been commonly estimated by a model-based approach of simulating global  
34 aerosol amount, distribution, and characteristics, and processing the predicted global aerosol distribution by a  
35 radiation model. Global aerosol simulations are subject to large uncertainties in emissions, transport, gas-to-aerosol

36 conversion, aerosol aging, aerosol mixing state, and wet and dry deposition (Bond et al., 2004; Ma et al., 2012). The  
37 large spread among direct aerosol forcing estimates (Myhre et al., 2013a) is attributable largely to these simulation  
38 uncertainties. Plus, processing the calculated aerosol distribution by a radiation model requires the specification of  
39 parameters such as the single scattering albedo (SSA) of organic aerosol which has been treated as 0.96-1.0 at 550  
40 nm in the modeling community (Myhre et al. 2013b) but might actually be much lower (e.g., 0.85 estimated by  
41 Magi 2009; 2011). Attempts have been made to bypass some of these uncertainties and constrain calculated aerosol  
42 optical properties by observations (Chung et al., 2005; Bellouin et al., 2008; Myhre, 2009; Su et al., 2013) but these  
43 semi-empirical studies are not sufficient to validate the model based estimates given heavy model dependence. In  
44 particular, the anthropogenic fraction of aerosol amount was obtained entirely from aerosol simulations (Chung et al.,  
45 2005; Myhre, 2009; Su et al., 2013) or by utilizing the fine-mode fraction (FMF) of satellite-derived AOD (Aerosol  
46 Optical Depth) over ocean (Bellouin et al., 2008; Chung et al., 2005). Over the land, where most anthropogenic  
47 aerosols are located, no study constrained the anthropogenic fraction by observations yet.

48 Aerosols have different sizes, and typically follow a bimodal structure in terms of fine mode and coarse  
49 mode (Kim et al., 2007; Viskari et al., 2012). Fine-mode aerosols usually have submicron sizes in diameter and  
50 these small particles are mostly anthropogenic. In this study, we provide observational estimates of direct fine-mode  
51 aerosol radiative effect (i.e., anthropogenic + natural forcing due to all the fine-mode aerosols). In particular, we  
52 constrain total AOD, SSA, and the asymmetry parameter by observations as in previous semi-empirical studies  
53 (Chung et al., 2005; Myhre, 2009; Su et al., 2013). In addition, we use observations to constrain the aerosol vertical  
54 profile, and the FMF of AOD over land as well as ocean. There is some use of simulated aerosol to fill up  
55 observation gaps in our study but the use is highly limited, and we address the uncertainty due to the use of  
56 simulation. When our observational estimates are compared to the simulated fine-mode aerosol radiative effects, one  
57 can obtain additional insights into biases and uncertainties in the aerosol forcing estimates from aerosol simulations.

58 Atmospheric aerosols consist of carbonaceous, sulfate, nitrate, sea salt and dust aerosols. The first three  
59 types of aerosols are fine-mode particles which are mostly anthropogenic while a sizable portion of sea salt and dust  
60 aerosols are also in the fine mode. Thus, offering observational estimates of fine-mode aerosol radiative effect is an  
61 important advance but is not sufficient in understanding the biases in the aerosol forcing estimates from aerosol  
62 simulations. In the present study, we will use observations to constrain the fine-mode sea salt and dust AODs as  
63 well, and offer estimates of aerosol radiative effect due to fine-mode sea salt and dust aerosols.

## 64 2. Data

65 In section 4 and Table 1, aerosol direct radiative effects (DRE) will be computed for three cases: (i) for  
66 total aerosols, (ii) for the fine mode (including natural fine-mode particles), and (iii) for fine mode sea-salt and dust.  
67 The total and fine-mode AOD are based on observations, as explained in Section 2.1. The other aerosol optical  
68 properties needed for the DRE calculations are derived as follows:

69 • The asymmetry parameter (ASY), SSA and the Co-albedo Ångström Exponent (CAI\_AE) for the total aerosols are  
70 derived by nudging GOCART simulated values towards AERONET data (Section 2.2). The spectral dependence of  
71 ASY is addressed as in Chung et al. (2005).

- 72 • The fine-mode aerosol DRE is computed as the difference between the total and coarse mode DREs. The coarse-  
73 mode ASY, SSA and CAI\_AE are derived from GOCART simulations, as explained in Section 2.3.  
74 • For computing the DRE due to fine-mode sea-salt and dust, ASY, SSA and CAI AE are derived from GOCART  
75 simulations (Section 2.3).

76 The datasets used to derive this information are explained in the following. All the datasets used in this  
77 study are monthly means.

## 78 2.1 Global observational data

79 AOD is a common measure of aerosol amount. AERONET (Aerosol Robotic Network; Holben et al., 1998)  
80 AOD is known to be the most accurate global-scale product. However, AERONET sites are non-uniformly  
81 distributed over the globe while less-reliable satellite (MODIS and MISR) AODs have nearly full global coverage.  
82 We follow the approach of Chung et al. (2005) and Lee and Chung (2013) in nudging or adjusting the satellite AOD  
83 towards AERONET AOD to construct globally-reliable AOD from 2001 to 2010. See Chung et al. (2005) and Lee  
84 and Chung (2013) for the visual effects of the nudging. Fig. 1A shows this adjusted AOD. Also, AOD Ångström  
85 exponent from 2001 to 2010 is derived by adjusting the satellite data towards AERONET data as in Lee and Chung  
86 (2013).

87 Fine-mode AOD (fAOD) at 500 nm from 2001 to 2010 are obtained by the approach in Lee and Chung  
88 (2013), except that instead of directly using the monthly AERONET FMF data we used the monthly AERONET  
89 fAOD (from the direct sun measurements and the Spectral Deconvolution Algorithm as in Lee and Chung) and total  
90 AOD to derive the FMF. Like in Lee and Chung (2013), we convert AOD Ångström exponent data into FMF data,  
91 and nudge this FMF data towards AERONET FMF data to derive reliable FMF and thus fine-mode AOD over the  
92 globe. Note that the definition of fine mode in the present study thus follows that by the AERONET Spectral  
93 Deconvolution Algorithm as in O'Neill et al. (2003) and Lee and Chung (2013). Coarse-mode AOD at 500 nm is  
94 obtained by subtracting fine-mode AOD from total AOD at 500 nm.

95 We computed the 2001-2010 average for each calendar month at the T42 resolution. In these datasets, the  
96 observational data gaps are filled by the GOCART simulation (Chin et al., 2002) as in Lee and Chung (2013).  
97 These data gaps are predominantly confined to the polar regions, and are even fewer in polar summer.

98 We obtain fAOD at 550 nm by subtracting coarse-mode AOD at 500 nm from AOD at 550 nm, assuming  
99 that coarse-mode AOD does not change from 500 nm to 550 nm. That is,  $fAOD_{550} = fAOD_{500} + (AOD_{550} -$   
100  $AOD_{500})$ . Total AOD at any wavelength is obtained by combining AOD at 550 nm and AOD Ångström Exponent.

## 101 2.2 Global semi-observational data

102 To compute the direct aerosol radiative effect, aerosol optical characteristics, such as SSA (Single  
103 Scattering Albedo), must be specified. We construct a global distribution of SSA by nudging global model-  
104 simulated (Chin et al., 2002) SSA towards AERONET SSA. We apply a similar procedure to ASY.

105 550 nm SSA, 550 nm ASY, CAL\_AE (Co-albedo Ångström Exponent; Co-albedo = 1-SSA) for total  
 106 (natural + anthropogenic) aerosols are obtained by nudging the GOCART simulation (Chin et al., 2002) towards  
 107 AERONET data. Specifically, for ASY and CAL\_AE the following nudging equation is used:

$$108 \quad N\_ASY_j = G\_ASY_j + \frac{\sum_i \frac{AERONET\_ASY_i - G\_ASY_i}{d_{j,i}^4}}{\sum_i \frac{1}{d_{j,i}^4}} \quad (1)$$

109 where  $N\_ASY_j$  is the adjusted new value of ASY at grid  $j$ ;  $AERONET\_ASY_i$  is an AERONET ASY at station  $i$ ;  $d_{j,i}$   
 110 is the distance between  $j$  and  $i$ ; and  $G\_ASY_i$  is the GOCART ASY at the grid box containing AERONET $_i$ . Here the  
 111 AERONET data and the GOCART simulation are on the T42 grids.

112 For SSA, the following equation is used:

$$113 \quad (1 - N\_SSA_j) = (1 - G\_SSA_j) \times \frac{\sum_i \frac{1 - AERONET\_SSA_i}{d_{j,i}^4}}{\sum_i \frac{1 - G\_SSA_i}{d_{j,i}^4}} \quad (2).$$

114 Another way to interpret the above equations (Eq. 1, 2) is that the GOCART simulation is an interpolation tool. The  
 115 equation for SSA differs from that for ASY or CAL\_AE, because SSA cannot be negative, and its value goes down  
 116 from 1.0. The above equations are applied for each grid and each calendar month. The final values are the  
 117 simulation nudged towards AERONET values. Please note that these above equations (Eq. 1 & 2) were also used in  
 118 Chung et al. (2005) but a clear explanation was not given in that study.

119 Before combining the GOCART simulation and AERONET data, the 2001-2010 average was calculated  
 120 from the monthly Level 2.0 AERONET data for each calendar month. The average of the AERONET SSA or ASY  
 121 was AOD-weighted. Then, SSA and ASY at 550 nm were obtained from the neighboring wavelength values through  
 122 linear interpolation. AERONET CAL\_AE was obtained by the 2001-2010 SSA averages at 440, 675 and 870 nm for  
 123 each calendar month. Please note that AERONET only gives level 2 quality SSA when AOD at 440 nm >0.4, and  
 124 therefore many regions of the earth do not have AERONET SSA data.

125 The products from combining the GOCART simulation and AERONET data are semi-observational and  
 126 we address the model dependence as follows.

127 SSA, apart from AOD, is the most influential parameter in aerosol direct forcing (Chung, 2012). We first  
 128 generated three different sets of simulated SSA:

$$129 \quad SSA1 = (0.19 \times BC\_AOD + 0.85 \times OA\_AOD + 1.0 \times sulfate\_AOD + 1.0 \times sea-salt\_AOD + 0.96 \times dust\_AOD) / total\_AOD;$$

$$130 \quad SSA2 = (0.14 \times BC\_AOD + 0.8 \times OA\_AOD + 1.0 \times sulfate\_AOD + 1.0 \times sea-salt\_AOD + 0.96 \times dust\_AOD) / total\_AOD; \text{ and}$$

$$131 \quad SSA3 = (0.19 \times BC\_AOD + 0.98 \times OA\_AOD + 1.0 \times sulfate\_AOD + 1.0 \times sea-salt\_AOD + 0.96 \times dust\_AOD) / total\_AOD.$$

132  
 133  
 134  
 135 BC\_AOD above refers to the GOCART BC AOD at 550 nm. We chose parameters (e.g., 0.19 for BC SSA) in the  
 136 above three SSA equations from various observational studies (e.g., Magi, 2009; Magi, 2011). Additionally, in  
 137 SSA2 (more absorbing case), we doubled the magnitude of BC AOD, given a notion (e.g., Chung et al., 2012) that  
 138 simulated BC is significantly underestimated. We use the above three sets of simulated SSA in order to produce an

139 initial estimate of the uncertainty in simulated SSA. Then, we nudged the 3 sets of simulated SSA towards the same  
140 AERONET SSA, which gave 3 sets of semi-observational SSA. Finally, we computed the average, maximum and  
141 minimum SSAs from the three sets of SSA over each grid and each calendar month, and then re-generated three sets  
142 of SSA (average: baseline; maximum; and minimum; see Fig. 2). This re-generation increases the global-average  
143 SSA difference between the least absorbing and most absorbing cases. We do this re-generation in an attempt to  
144 fully bracket the simulated SSA uncertainty. The last procedure (i.e., re-generation) assures that the final three sets  
145 of SSA depend insignificantly on the initial estimate of the simulated SSA uncertainty.

146 Simulated ASY at 550 nm and CAI\_AE are computed as follows.

$$147 \text{ASY} = (0.6 \times \text{CA\_SAOD} + 0.7 \times \text{sulfate\_SAOD} + 0.75 \times \text{sea-salt\_SAOD} + 0.75 \times \text{dust\_SAOD}) / \text{total\_SAOD}.$$

148 CA\_SAOD here refers to Carbonaceous Aerosol (i.e., BC+OA) SAOD (Scattering AOD) at 550 nm from GOCART.

$$149 \text{CAI\_AE} = (-0.53 \times \text{CA\_AOD} + 2.215 \times \text{dust\_AOD}) / \text{total\_AOD},$$

150 where CA\_AOD refers to CA AOD. The chosen parameters (e.g., 2.215) in the ASY and CAI\_AE equations are  
151 from preliminary AERONET data analysis. These simulated ASY and CAI\_AE were nudged towards AERONET  
152 data as explained earlier. We do not address the model dependence on ASY or CAI\_AE, since its impact on aerosol  
153 forcing is tiny compared to the impact of SSA uncertainty. To be sure, we re-generated the ASY using doubled BC  
154 AOD while holding other components (such as SSA) fixed, and found that the global direct aerosol effect changes  
155 by less than  $0.002 \text{ Wm}^{-2}$ .

156 The GOCART simulations were prepared as follows. We used sea salt AOD from Chin et al. (Chin et al.,  
157 2002), and BC (black carbon), OA (Organic Aerosol), dust and sulfate AODs from the Giovanni website  
158 ([http://gdata1.sci.gsfc.nasa.gov/daac-bin/G3/gui.cgi?instance\\_id=neespi](http://gdata1.sci.gsfc.nasa.gov/daac-bin/G3/gui.cgi?instance_id=neespi)), which contains GOCART model output  
159 from 2000 to 2007. These AODs are monthly means at 550 nm. Then, the climatological seasonal cycle for the  
160 available data period was computed. We used these simulated AOD values to compute the simulated SSA, ASY  
161 and CAL\_AE.

## 162 2.3 Global simulations

163 For coarse-mode aerosols, we assumed ASY to be 0.75 and AOD Ångström exponent to be 0.0. For 550  
164 nm SSA and CAL\_AE, we rely entirely on the GOCART simulations as follows:  $\text{SSA} = (1.0 \times \text{sea-}$   
165  $\text{salt\_AOD} + 0.96 \times \text{dust\_AOD}) / \text{IAOD}$ , where dust\_AOD refers to GOCART dust AOD and IAOD refers to GOCART  
166 dust and sea salt AODs combined.  $\text{CAL\_AE} = 2.215 \times \text{dust\_AOD} / \text{IAOD}$ . Although we rely entirely on simulated  
167 SSA for coarse-mode aerosols, we find very small the coarse-mode aerosol radiative effect uncertainty resulting  
168 from simulated SSA. For instance, when we change the dust AOD by 35%, the difference in coarse-mode aerosol  
169 radiative effect is only  $0.01 \text{ Wm}^{-2}$ .

170 For fine-mode sea salt and dust aerosols, we assumed ASY to be 0.6 and AOD Ångström exponent to be  
171 1.85. For 550 nm SSA and CAL\_AE, we rely entirely on simulated fAODs as follows:

$$172 \text{SSA} = (1.0 \times \text{sea-salt\_fAOD} + 0.96 \times \text{dust\_fAOD}) / \text{fAOD},$$

173 where dust\_fAOD refers to dust fAOD and fAOD refers to dust and sea salt fAODs combined.  
174  $\text{CAL\_AE} = 2.215 \times \text{dust\_fAOD} / \text{fAOD}$ .

175           These simulated aerosol optical properties were used in the MACR model runs, leading to the results in  
176 Table 1.

## 177 **2.4 Vertical profile**

178           Aerosol vertical profiles are obtained from the space-borne CALIOP lidar (Liu et al., 2009). To construct  
179 the profile, we used the daytime CALIPSO lidar level 2.0 data (Liu et al., 2009) from June 2006 to Oct. 2011. We  
180 processed the level 2.0 data, and obtained clear-sky aerosol extinction coefficient at 532 nm at the T42 spatial  
181 resolution and 500 m MACR model vertical resolution. We filled the data gaps using available neighboring data  
182 through linear interpolation. We then computed the climatological seasonal cycle for the entire available data period.  
183 Over some grids and calendar months, the aerosol extinction coefficient has extremely low magnitudes, in which  
184 case, the PBL profile as in Chung et al. (Chung et al., 2012) is applied. The threshold for applying the PBL profile  
185 is a vertically-summed aerosol extinction coefficient of 0.03. Note that a vertically-summed aerosol extinction  
186 coefficient of 0.03 is associated with a very small amount of aerosol and the effect of these aerosols on global  
187 aerosol direct effect is very small. Also note that the aerosol vertical profile from CALIPSO is scaled to match the  
188 AOD observations obtained by integrating AERONET, MODIS and MISR data (as shown in Fig. 1A) since the  
189 latter observations describe clear-sky AOD too and give better accuracy. The clear-sky aerosol profile from  
190 CALIPSO is assumed to be applied to an entire T42 grid in the MACR model.

191           To adjust the magnitude of AOD over cloud by CALIPSO data, we use the daytime CALIPSO lidar level  
192 3.0 data (Winker et al., 2013), which are globally-gridded ( $5^\circ \times 2^\circ$ ) monthly mean data spanning from June 2006 to  
193 Jan. 2012. Specifically, we use the CALIPSO level 3.0 derived ratio of clear-sky AOD to above-cloud AOD to  
194 modify the aerosol amount over cloud over each grid cell in the MACR model. The level 3.0 data have gaps. Again,  
195 the data gaps were filled using a linear interpolation, then the data was converted into the T42 grids, and the  
196 climatological seasonal cycle was obtained before the use in MACR model.

197           For coarse-mode aerosols, we apply the same profiles given a lack of observations. Because coarse-mode  
198 aerosols are not very absorbing, the effect of the vertical profile is very small (see Choi and Chung, 2014).

## 199 **3. Radiation model**

200           We use the Monte-Carlo Aerosol Cloud Radiation (MACR) model as in Choi and Chung (2014), except  
201 that we improved the low cloud height in the model using the CALIPSO level 2.0 data. As in Choi and Chung  
202 (2014), the height of low cloud bottom is set to 750 m above the ground. The low cloud top height is set to 1250 m,  
203 when the maximum low cloud height over a  $5^\circ \times 2^\circ$  grid (and during a whole month) from CALIPSO data is 750m ~  
204 1750m. When the CALIPSO maximum low cloud height exceeds 1750 m, the low cloud top height in the model is  
205 set to 1750 m above the ground.

206           This model was built upon the so-called Monte Carlo Independent Column Approximation (McICA)  
207 approach (Pincus et al., 2003); uses a set of satellite observations to describe multi-layer cloud, surface albedo, and  
208 stratospheric column ozone; and uses ERA-Interim Reanalyses (Dee et al., 2011) to describe the precipitable water.

209 An earlier version has undergone comprehensive validation of the simulated fluxes at the TOA and at the surface  
210 over 100 land and island stations (agreement with observations is within a few  $\text{Wm}^{-2}$ ) (Kim and Ramanathan, 2008).  
211 Only short-wave radiation is considered here.

#### 212 **4. Aerosol direct radiative effect**

213 We first address the direct aerosol radiative effect (forcing due to natural and anthropogenic aerosols). We  
214 incorporated the integrated global aerosol data (as explained in section 2) into the MACR model. Fig. 1B shows  
215 the direct aerosol radiative effect as estimated by the MACR model. The direct aerosol radiative effect in Fig. 1B  
216 also incorporates that aerosol amount over cloud might differ from that at the same height in clear skies in the same  
217 region. The CALIOP lidar is able to retrieve aerosol amount over cloud as well as in clear skies, and so we used this  
218 lidar data to constrain the aerosol amount over cloud (as explained in section 2.4) in computing the direct aerosol  
219 radiative effect. This procedure could be important since radiation modeling studies showed that the sensitivity of  
220 aerosol forcing to the aerosol vertical profile arises mainly as a consequence of the location of absorbing particles  
221 relative to cloud (Choi and Chung, 2014). On the other hand, cloud is brighter than most surfaces during daytime,  
222 and this could create a low bias in aerosol amount over cloud, as retrieved by the CALIOP lidar (Chepfer et al., 2013;  
223 Hunt et al., 2009; Kacenelenbogen et al., 2014; Vaughan and coauthors, 2009). To be sure, we re-computed the  
224 aerosol radiative effect assuming equal amounts between clear skies and over cloud, and found that the radiative  
225 effect only increases by  $0.03 \text{ Wm}^{-2}$  in global average.

226 Next, we estimate fine-mode aerosol radiative effect. Since the FMF of aerosols over land is difficult to  
227 accurately retrieve from satellites, past semi-empirical estimates (Bellouin et al., 2008; Myhre, 2009) only used the  
228 FMF of AOD from satellite observations over the ocean. In contrast, AERONET data provide relatively reliable  
229 FMF over both land and ocean (with the AERONET data being predominantly over land). Following the approach  
230 of Lee and Chung (2013) satellite data are nudged toward AERONET data to construct global FMF and thus fine-  
231 mode AOD (see section 2.1 for details). Fig. 3A shows this fine-mode AOD, which, as expected, is largest over  
232 industrial and biomass burning areas.

233 Fig. 3B shows the estimated fine-mode direct radiative effect as the difference between the coarse-mode  
234 and total (coarse + fine modes) aerosol radiative effect. Fine-mode radiative effect is negative almost everywhere,  
235 except over the eastern equatorial Atlantic, the Sahara, and the Arabian Desert. These areas of positive forcing  
236 result from highly absorbing particles above highly reflective surfaces or low cloud. The global average of the fine-  
237 mode direct radiative effect is estimated as  $-0.46 \text{ Wm}^{-2}$ . In this computation, aerosol simulation using GOCART  
238 was used to provide interpolation for aerosol optical characteristics, such as SSA. To quantify uncertainty in the  
239 model dependence, two sets of additional simulations were conducted, representing lower and upper limits of  
240 absorption efficiency (see section 2.2 and Fig. 2). Fine-mode radiative effect is estimated to range between  $-0.54$   
241  $\text{Wm}^{-2}$  and  $-0.39 \text{ Wm}^{-2}$ , corresponding to these two limits (Table 1). Aerosol simulations yielding fine-mode

242 radiative effect outside of the  $-0.54 \sim -0.39 \text{ Wm}^{-2}$  range can be considered as inconsistent with observational  
243 constraints.

## 244 **5. Fine-mode fraction (FMF) of sea salt and dust AODs**

245 The fine-mode direct radiative effect estimate, as shown in Fig. 3B, includes the contribution from natural fine-  
246 mode sea salt and dust aerosols. To subtract this contribution from the fine-mode direct radiative effect estimate, we  
247 address the FMF of sea salt and dust AODs here. Instead of using simulated fine-mode sea salt and dust AOD (and  
248 thus being 100% subject to model uncertainties), we use observed coarse-mode AOD  $\times \frac{SD\_FMF}{1-SD\_FMF}$ , where  $SD\_FMF$   
249 refers to the simulated FMF of sea salt + dust AOD. An underlying assumption therein is that coarse-mode AOD  
250 results only from sea salt and dust aerosols. We obtain the observed coarse-mode AOD by subtracting fine-mode  
251 AOD from total AOD where the fine-mode and total AODs were obtained by integrating AERONET, MODIS and  
252 MISR data (see section 2.1). On rare occasions,  $\frac{SD\_FMF}{1-SD\_FMF}$  becomes unrealistically large. To prevent this, we limit  
253 fine-mode sea salt and dust AOD to be  $< 99\%$  of total fine-mode AOD.

254 For simulated FMF, we used AOD (at 550 nm) simulations from GOCART, the Spectral Radiation-Transport  
255 Model for Aerosol Species (SPRINTARS), the Tracer Model 5 (TM5) and ModelE2-TOMAS (briefly ModelE2  
256 here). The SPRINTARS output is from the AeroCom (Aerosol Comparisons between Observations and Models)  
257 Phase II (Schulz et al., 2009) hindcast experiments and the TM5 outputs are from the AeroCom Phase III. The  
258 ModelE2-TOMAS simulation was performed using the Two-Moment Aerosol Sectional (TOMAS) microphysics  
259 module incorporated into the state-of-the-art general circulation model GISS ModelE2 (Lee et al., 2015). TOMAS  
260 module represents aerosol size distribution in many size categories or “bins” covering 10nm to 10 $\mu\text{m}$ . We used a  
261 Fast-TOMAS module (Lee and Adams, 2012) with a 15 bin version here, since Fast TOMAS reduces the  
262 computational burden by 2-3 times while well preserving the capability of computing fine-mode fraction compared  
263 to the original TOMAS model with 30 bins. The fine-mode fraction of dust and sea-salt aerosols from ModelE2-  
264 TOMAS was calculated by converting the mass output to AODs, and then applying the Spectral Deconvolution  
265 Algorithm (SDA) used in AERONET retrievals (O'Neill et al., 2003) to the AODs in order to create FMF consistent  
266 with AERONET FMF. A Mie-scattering code was used to compute size-resolved AOD at 380, 440, 500, 675 and  
267 870 nm. Refractive indices for dust and sea-salt are taken from Optical Properties of Aerosol and Clouds (OPAC)  
268 dataset (Hess et al., 1998). For other models, we calculated FMF using AODs from fine-mode aerosols and coarse-  
269 mode aerosols.

270 The ModelE2-TOMAS simulation was nudged with wind from MERRA (Modern Era Retrospective-analysis  
271 for Research and Applications) reanalysis from 2003 to 2005 after 3 years of spin-up. The simulation period for  
272 ModelE2-TOMAS is 2003-2005, and that for TM5, SPRINTARS and GOCART are 2001-2010, 2001-2008, and  
273 2000-2007, respectively. Climatological AODs for each of 4 models were obtained by computing the average over  
274 the aforementioned simulation period for each calendar month.



275 Fig. 4 is displayed to compare various simulated FMFs with the observed FMF. First, we assess which  
276 simulation performs the best in simulating dust FMF by looking at the simulated FMFs (including FMF of non-dust  
277 particles) over dust dominated places where we use AERONET observations to validate the simulated FMFs. Dust-  
278 dominated AERONET sites in Fig. 4A were selected with the following criteria: 550 nm FMF < 0.3, AAE  
279 (Absorption Ångström Exponent) > 2.0 and 550 nm AAOD (Absorption AOD) > 0.03. We again followed the  
280 approach by Lee and Chung (2013) in computing AERONET FMF, AAE and AAOD. Please note that in Fig. 4 we  
281 used climatological means for each calendar month; again for FMF we used mean AODs to compute the FMF  
282 instead of averaging FMFs. Fig. 4B suggests that models tend to over-estimate dust FMF, at least over dust-  
283 dominated places, as previously pointed out by Kok (2011).

284 Regarding sea salt FMF, we look at the simulated sea salt FMFs and observed total FMF over relatively pristine  
285 oceans (Fig. 4C). Organic and sulfate aerosols can be over remote oceans (Shank et al., 2012) in addition to fine-  
286 mode sea salt. Fig. 4C shows large disagreements between sea salt FMF simulations, where one of the models (i.e.,  
287 GOCART) clearly overestimates sea salt FMF given that the simulated sea salt FMF is near the total FMF from  
288 observations. In view of this, we scale down the simulated fine-mode dust FMF and mix sea salt FMF simulations  
289 to calculate FMF of sea salt.

290 We scale down the simulated dust FMF and mix sea salt FMF simulations by having multiple estimates (best  
291 estimate and sensitivity runs) to address the uncertainty in simulated FMF. The FMF of sea salt + dust AOD for our  
292 best estimate (i.e., baseline) is prepared using ModelE2 as follows. We scale up the coarse-mode dust AOD by 1.16  
293 times and scale down the fine-mode dust AOD by 0.56 times so that ModelE2 would match AERONET FMF and  
294 AOD over dust-dominated sites. We scale down sea salt AOD (both fine and coarse modes) by 0.6 times so that the  
295 total AOD from ModelE2 matches AERONET data over sea salt dominated sites. We use ModelE2 for the best  
296 estimate since this model has an advanced size distribution description and uses the SDA to divide the AOD into  
297 fine-mode and coarse-mode components. For sensitivity run 1, we replace the ModelE2 dust AOD by the GOCART  
298 dust AOD where the coarse-mode dust AOD is scaled up by 1.3 times and the fine-mode dust AOD is scaled down  
299 by 0.74 times. For sensitivity run 2, we use the baseline set-up except that for sea salt AOD we equally mix the  
300 outputs from GOCART, TM5 and ModelE2.

301 *Scaling the simulated dust FMF to match AERONET FMF over dust-dominated sites may still have an*  
302 *overestimation or underestimation of dust FMF outside of dust dominated regions. Plus, dust-dominated regions*  
303 *have non-dust particles, and thus the scaled dust FMF might still underestimate or overestimate dust FMF even over*  
304 *dust dominated regions. This is why we conduct sensitivity runs even after the scaling of the simulated dust FMF.*  
305

## 306 **6. Implications for global direct aerosol radiative forcing**

307 We estimate the direct radiative effect due to fine-mode sea salt and dust aerosols at  $-0.35$  ( $-0.44 \sim -0.26$ )  
308  $\text{Wm}^{-2}$  (Table 1). The spatial pattern is shown in Fig. 5. As mentioned in section 5, our estimate of fine-mode sea  
309 salt and dust aerosols might be too large or too small over some areas. Possible over-estimation or under-estimation

310 is likely reduced in global average, and so we focus on global averages as shown in Table 1. The global direct  
311 radiative effect of  $-0.35 \text{ Wm}^{-2}$  is quite large. In those studies where fine-mode sea salt and dust aerosols were  
312 assumed to be negligible, the aerosol direct forcing estimates would have been that much more negative than in  
313 reality.

314 When we remove the contribution of fine-mode sea salt and dust aerosols from the fine-mode radiative  
315 effect, we end up with aerosol radiative effect due to total (i.e., anthropogenic + natural) carbonaceous, sulfate and  
316 nitrate aerosols. As Fig. 6A shows, this radiative effect is large and positive over Africa and the downstream areas  
317 where biomass burning is the major source. The forcing is also conspicuously positive over the Sahara (Fig. 6A),  
318 partly because biomass burning aerosols in the Sahel are advected northwards in boreal winter (Haywood et al.,  
319 2008) and bright desert surfaces turn the forcing positive. Fig. 6B shows that these advected aerosols have a  
320 relatively small forcing in the atmosphere due to smaller aerosol amounts. Outside of Africa and the downstream  
321 areas, the forcing is a mixture of positive and negative values, and negative values slightly outweigh positive values.  
322 The global average (including Africa) of the TOA forcing (as shown in Fig. 6A) is  $-0.11 \text{ Wm}^{-2}$  with an uncertainty  
323 range of  $-0.28 \sim +0.05 \text{ Wm}^{-2}$  which results from  $-0.54+0.26 \sim -0.39+0.44 \text{ Wm}^{-2}$ .

324 The consensus of global aerosol direct radiative forcing as shown in the 5<sup>th</sup> IPCC report is  $-0.35 \text{ Wm}^{-2}$   
325 (Myhre et al., 2013a), and this includes a dust forcing of  $-0.10 \text{ Wm}^{-2}$ . Thus, the IPCC estimate is that  
326 anthropogenic carbonaceous, sulfate and nitrate aerosols pose a radiative forcing of  $-0.25 \text{ Wm}^{-2}$ , while our  
327 observational estimate of total (anthropogenic + natural) carbonaceous, sulfate and nitrate aerosol forcing is  $-0.11$   
328  $\text{Wm}^{-2}$ . The anthropogenic fraction (or pre-industrial fraction) of carbonaceous, sulfate and nitrate aerosols is  
329 uncertain. Black carbon, the only warming aerosol species in carbonaceous aerosol (black carbon + organic aerosol),  
330 sulfate and nitrate aerosol is known to be more anthropogenic than organic aerosols are (Bond et al., 2011). If the  
331 anthropogenic fraction of black carbon is similar to that of nitrate and sulfate aerosol, the aerosol direct radiative  
332 forcing becomes  $> -0.11 \text{ Wm}^{-2}$  in our observational estimation, which means that aerosol direct forcing is less  
333 negative than the consensus as expressed in the 5<sup>th</sup> IPCC report.

334 Our observational approach makes the results subject to observation errors. AERONET SSA, in particular,  
335 is subject to potentially significant uncertainties due to various assumptions used in the retrieval algorithms. Thus,  
336 the uncertainty in our estimates of fine-mode forcing, e.g., might be larger than  $-0.54 \sim -0.39 \text{ Wm}^{-2}$ . However,  
337 studies (Eck et al., 2010; Leahy et al., 2007) showed that AERONET SSA is higher or lower than in-situ  
338 measurements depending on location, season, in-situ measurement device, etc. Furthermore, in-situ measurements  
339 are also subject to uncertainties, and so the difference between the AERONET SSA and in-situ measured SSA is not  
340 necessarily due only to the AERONET data error. Overall, we believe that AERONET observations likely have  
341 smaller biases and provide more credible results than aerosol simulations. At least, our observational approach  
342 offers an independent estimate than pure aerosol simulations.

## 343 **Acknowledgment**

344 The authors are thankful to P. Adams of Carnegie Mellon University and N.T. O'Neill at Canadian Network for the  
345 Detection of Atmospheric Change for valuable inputs. This study was funded by the National Science Foundation  
346 (AGS-1455759).  
347

348 **References**

- 349 Bellouin, N., Jones, A., Haywood, J., and Christopher, S. A.: Updated estimate of aerosol direct radiative forcing  
350 from satellite observations and comparison against the Hadley Centre climate model, *Journal of Geophysical*  
351 *Research: Atmospheres*, 113, D10205, 2008.
- 352 Bond, T. C., Streets, D. G., Yarber, K. F., Nelson, S. M., Woo, J.-H., and Klimont, Z.: A technology-based global  
353 inventory of black and organic carbon emissions from combustion, *J. Geophys. Res.*, 109, D14203, 2004.
- 354 Bond, T. C., Zarzycki, C., Flanner, M. G., and Koch, D. M.: Quantifying immediate radiative forcing by black  
355 carbon and organic matter with the Specific Forcing Pulse, *Atmos. Chem. Phys.*, 11, 1505-1525, 2011.
- 356 Chepfer, A., Cesana, G., Winker, M. A., Getzewich, B., Vaughan, K. A., and Liu, Z.: Comparison of two different  
357 cloud climatologies derived from CALIOP-attenuated backscattered measurements (Level 1): The CALIPSO-ST  
358 and the CALIPSO-GOCCP, *Journal of Atmospheric and Oceanic Technology*, 30, 725–744, 2013.
- 359 Chin, M., Ginoux, P., Kinne, S., Torres, O., Holben, B. N., Duncan, B. N., Martin, R. V., Logan, J. A., Higurashi, A.,  
360 and Nakajima, T.: Tropospheric aerosol optical thickness from the GOCART model and comparisons with  
361 satellite and sun photometer measurements, *J. Atmos. Sci.*, 59, 461-483, 2002.
- 362 Choi, J.-O. and Chung, C. E.: Sensitivity of aerosol direct radiative forcing to aerosol vertical profile, *Tellus B*, 66,  
363 2014.
- 364 Chung, C. E., Ramanathan, V., and Decremier, D.: Observationally constrained estimates of carbonaceous aerosol  
365 radiative forcing, *Proceedings of the National Academy of Sciences*, 109, 11624-11629, 2012.
- 366 Chung, C. E., Ramanathan, V., Kim, D., and Podgorny, I. A.: Global anthropogenic aerosol direct forcing derived  
367 from satellite and ground-based observations, *J. Geophys. Res.*, 110, D24207, 2005.
- 368 Chung, C. E.: Aerosol Direct Radiative Forcing: A Review, <http://dx.doi.org/10.5772/50248>, 2012.
- 369 Dee, D. P., Uppala, S. M., Simmons, A. J., Berrisford, P., Poli, P., Kobayashi, S., Andrae, U., Balmaseda, M. A.,  
370 Balsamo, G., Bauer, P., Bechtold, P., Beljaars, A. C. M., van de Berg, L., Bidlot, J., Bormann, N., Delsol, C.,  
371 Dragani, R., Fuentes, M., Geer, A. J., Haimberger, L., Healy, S. B., Hersbach, H., Hólm, E. V., Isaksen, L.,  
372 Kållberg, P., Köhler, M., Matricardi, M., McNally, A. P., Monge-Sanz, B. M., Morcrette, J. J., Park, B. K.,  
373 Peubey, C., de Rosnay, P., Tavolato, C., Thépaut, J. N., and Vitart, F.: The ERA-Interim reanalysis:  
374 configuration and performance of the data assimilation system, *Quarterly Journal of the Royal Meteorological*  
375 *Society*, 137, 553-597, 2011.
- 376 Eck, T. F., Holben, B. N., Sinyuk, A., Pinker, R. T., Goloub, P., Chen, H., Chatenet, B., Li, Z., Singh, R. P., Tripathi,  
377 S. N., Reid, J. S., Giles, D. M., Dubovik, O., O'Neill, N. T., Smirnov, A., Wang, P., and Xia, X.: Climatological  
378 aspects of the optical properties of fine/coarse mode aerosol mixtures, *J. Geophys. Res.*, 115, D19205, 2010.
- 379 Haywood, J. M. and Coauthors: Overview of the Dust and Biomass-burning Experiment and African Monsoon  
380 Multidisciplinary Analysis Special Observing Period-0, *Journal of Geophysical Research D: Atmospheres*, 113,  
381 2008.
- 382 Hess, M., Koepke, P., and Schult, I.: Optical Properties of Aerosols and Clouds: The Software Package OPAC, *B.*  
383 *Am. Meteorol. Soc.*, 79, 831-844, 1998.

384 Holben, B. N. and Coauthors: AERONET – A federated instrument network and data archive for aerosol  
385 characterization, *Remote Sensing Environment*, 66, 1-16, 1998.

386 Hunt, W. H., Winker, M. A., Vaughan, K. A., Powell, K. A., Lucker, P. L., and Weimer, C.: CALIPSO Lidar  
387 description and performance assessment, *Journal of Atmospheric and Oceanic Technology*, 26, 1214-1228, 2009.

388 Kacenelenbogen, M. S. and Coauthors: An evaluation of CALIOP/CALIPSO's aerosol-above-cloud (AAC)  
389 detection and retrieval capability, *Journal of Geophysical Research D: Atmospheres*, 119, 230-244, 2014.

390 Kim, J., Jung, C. H., Choi, B. C., Oh, S. N., Brechtel, F. J., Yoon, S. C., and Kim, S. W.: Number size distribution of  
391 atmospheric aerosols during ACE-Asia dust and precipitation events, *Atmospheric Environment*, 41, 4841-4855,  
392 2007.

393 Kim, D. and Ramanathan, V.: Solar radiation budget and radiative forcing due to aerosols and clouds, *J. Geophys.*  
394 *Res.*, 113, D02203, 2008.

395 Kok, J. F.: A scaling theory for the size distribution of emitted dust aerosols suggests climate models underestimate  
396 the size of the global dust cycle, *Proceedings of the National Academy of Sciences*, 108, 1016-1021, 2011.

397 Leahy, L. V., Anderson, T. L., Eck, T. F., and Bergstrom, R. W.: A synthesis of single scattering albedo of biomass  
398 burning aerosol over southern Africa during SAFARI 2000, *Geophys. Res. Lett.*, 34, L12814, 2007.

399 Lee, K. and Chung, C. E.: Observationally-constrained estimates of global fine-mode AOD, *Atmospheric Chemistry*  
400 *and Physics*, 13, 2907-2921, 2013.

401 Lee, Y. H. and Adams, P. J.: A Fast and Efficient Version of the Two-Moment Aerosol Sectional (TOMAS) Global  
402 Aerosol Microphysics Model, *Aerosol Science and Technology*, 46, 678-689, 2012.

403 Lee, Y. H., Adams, P. J., and Shindell, D. T.: Evaluation of the global aerosol microphysical ModelE2-TOMAS  
404 model against satellite and ground-based observations, *Geoscientific Model Development*, 8, 631-667, 2015.

405 Liu, Z. and Coauthors: The CALIPSO Lidar Cloud and Aerosol Discrimination: Version 2 Algorithm and Initial  
406 Assessment of Performance, *Journal of Atmospheric and Oceanic Technology*, 26, 1198-1213, 2009.

407 Ma, X., Yu, F., and Luo, G.: Aerosol direct radiative forcing based on GEOS-Chem-APM and uncertainties, *Atmos.*  
408 *Chem. Phys.*, 12, 5563-5581, 2012.

409 Magi, B. I.: Chemical apportionment of southern African aerosol mass and optical depth, *Atmos. Chem. Phys.*, 9,  
410 7643-7655, 2009.

411 Magi, B. I.: Corrigendum to "Chemical apportionment of southern African aerosol mass and optical depth"  
412 published in *Atmos. Chem. Phys.*, 9, 7643–7655, 2009, *Atmos. Chem. Phys.*, 11, 4777-4778, 2011.

413 Myhre, G., D. Shindell, et al.: Anthropogenic and Natural Radiative Forcing. In: *Climate Change 2013: The*  
414 *Physical Science Basis. Contribution of Working Group I to the Fifth Assessment Report of the*  
415 *Intergovernmental Panel on Climate Change, IPCC report, V, 2013a.*

416 Myhre, G., Samset, B. H., Schulz, M., Balkanski, Y., Bauer, S., Berntsen, T. K., Bian, H., Bellouin, N., Chin, M.,  
417 Diehl, T., Easter, R. C., Feichter, J., Ghan, S. J., Hauglustaine, D., Iversen, T., Kinne, S., Kirkevåg, A.,  
418 Lamarque, J. F., Lin, G., Liu, X., Lund, M. T., Luo, G., Ma, X., van Noije, T., Penner, J. E., Rasch, P. J., Ruiz,  
419 A., Seland, Ø., Skeie, R. B., Stier, P., Takemura, T., Tsigaridis, K., Wang, P., Wang, Z., Xu, L., Yu, H., Yu, F.,

420 Yoon, J. H., Zhang, K., Zhang, H., and Zhou, C.: Radiative forcing of the direct aerosol effect from AeroCom  
421 Phase II simulations, *Atmos. Chem. Phys.*, 13, 1853-1877, 2013b.

422 Myhre, G.: Consistency between satellite-derived and modeled estimates of the direct aerosol effect, *Science*, 325,  
423 187-190, 2009.

424 O'Neill, J. T., Eck, T. F., Smirnov, A., Holben, B. N., and Thulasiraman, S.: Spectral discrimination of coarse and  
425 fine mode optical depth, *Journal of Geophysical Research D: Atmospheres*, 108, 2003.

426 Pincus, R., Barker, H. W., and Morcrette, J.-J.: A fast, flexible, approximate technique for computing radiative  
427 transfer in inhomogeneous cloud fields, *J. Geophys. Res.*, 108, 4376, 2003.

428 Schulz, M., Chin, M., and Kinne, S.: The aerosol model comparison project, AeroCom, phase II: clearing up  
429 diversity, *IGAC Newsletter*, 2009. 2009.

430 Shank, L. M., Howell, S., Clarke, A. D., Freitag, S., Brekhovskikh, V., Kapustin, V., McNaughton, C., Campos, T.,  
431 and Wood, R.: Organic matter and non-refractory aerosol over the remote Southeast Pacific: Oceanic and  
432 combustion sources, *Atmospheric Chemistry and Physics*, 12, 557-576, 2012.

433 Su, W., Loeb, N. G., Schuster, G. L., Chin, M., and Rose, F. G.: Global all-sky shortwave direct radiative forcing of  
434 anthropogenic aerosols from combined satellite observations and GOCART simulations, *Journal of Geophysical  
435 Research D: Atmospheres*, 118, 655-669, 2013.

436 Vaughan, M. A. and coauthors: Fully automated detection of cloud and aerosol layers in the calipso lidar  
437 measurements, *Journal of Atmospheric and Oceanic Technology*, 26, 2034-2050, 2009.

438 Viskari, T., Asmi, E., Virkkula, A., Kolmonen, P., Petäjä, T., and Järvinen, H.: Estimation of aerosol particle  
439 number distribution with Kalman Filtering - Part 2: Simultaneous use of DMPS, APS and nephelometer  
440 measurements, *Atmospheric Chemistry and Physics*, 12, 11781-11793, 2012.

441 Winker, D. M., Tackett, J. L., Getzewich, B. J., Liu, Z., Vaughan, M. A., and Rogers, R. R.: The global 3-D  
442 distribution of tropospheric aerosols as characterized by CALIOP, *Atmos. Chem. Phys.*, 13, 3345-3361, 2013.

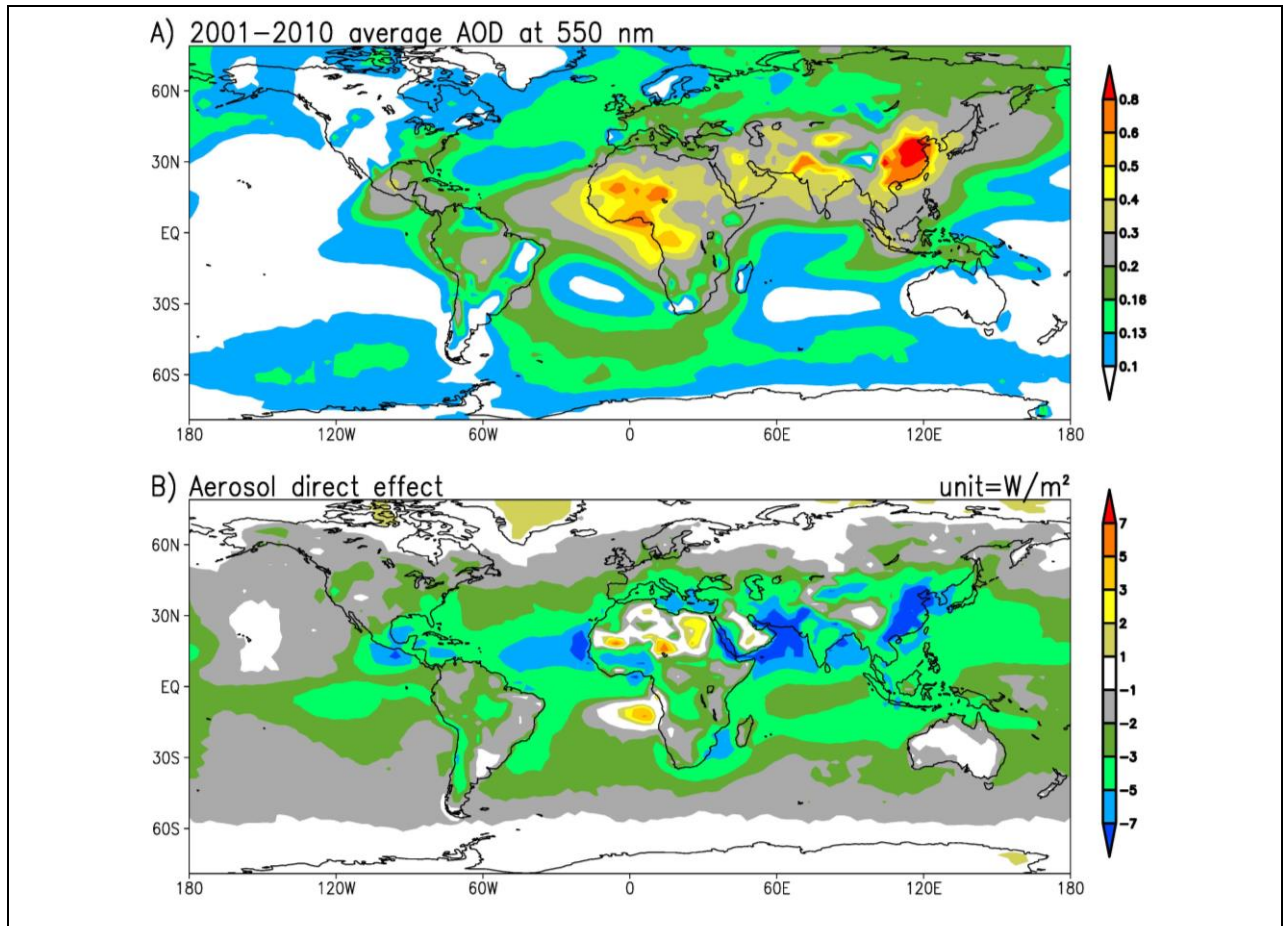
443

444 **Tables**

| Direct aerosol radiative effect                      | Run   | TOA (in<br>Wm <sup>-2</sup> ) | Atmosphere | Surface |
|--|---|-------------------------------|------------|---------|
| (Total) Direct aerosol radiative effect              |   | -2.28                         | +4.77      | -7.05   |
| Fine-mode radiative effect                           | baseline  | -0.46                         | +3.88      | -4.33   |
| Fine-mode radiative effect                           | sensitivity run 1: least absorbing case   | -0.54                         | +3.63      | -4.17   |
| Fine-mode radiative effect                           | sensitivity run 2: Most absorbing case  | -0.39                         | +4.08      | -4.47   |
| Fine-mode sea salt and dust radiative effect         | baseline: ModelE2 with reduced dust FMF   | -0.35                         | +0.23      | -0.58   |
| Fine-mode sea salt and dust radiative effect         | sensitivity run 1: reduced GOCART dust FMF + ModelE2 sea salt FMF                 | -0.26                         | +0.16      | -0.42   |
| Fine-mode sea salt and dust radiative effect         | sensitivity run 2: Reduced ModelE2 dust FMF + ModelE2/GOCART/TM5 mix sea salt FMF | -0.44                         | +0.26      | -0.70   |
| Fine-mode radiative effect without dust and sea salt | baseline  | -0.11                         | +3.64      | -3.75   |

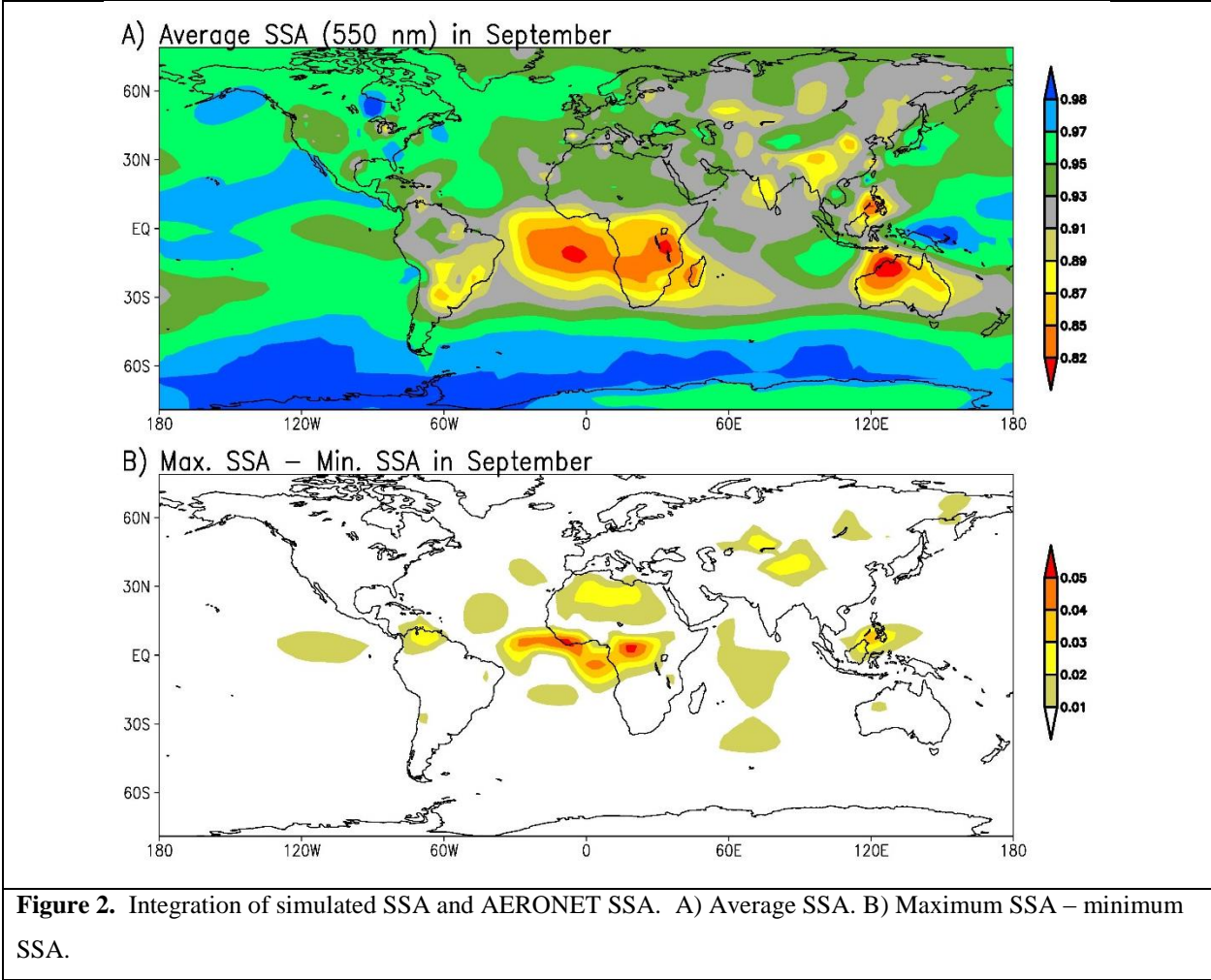
445  
446 **Table 1.** Global 2001-2010 average of aerosol radiative effect calculated with the MACR model. **In this table,**  
447 **natural aerosol radiative effects are included. All the aerosol radiative effect estimates made by the MACR model in**  
448 **this study include 3D cloud effects.**

449  
450



**Figure 1.** A) 2001-2010 mean 550 nm AOD obtained by integrating MODIS, MISR and AERONET AOD. B) 2001-2010 mean direct aerosol radiative effect at TOA, as estimated by a radiation model that includes observationally-derived surface albedo. The aerosol radiative effect estimate here includes natural aerosols.





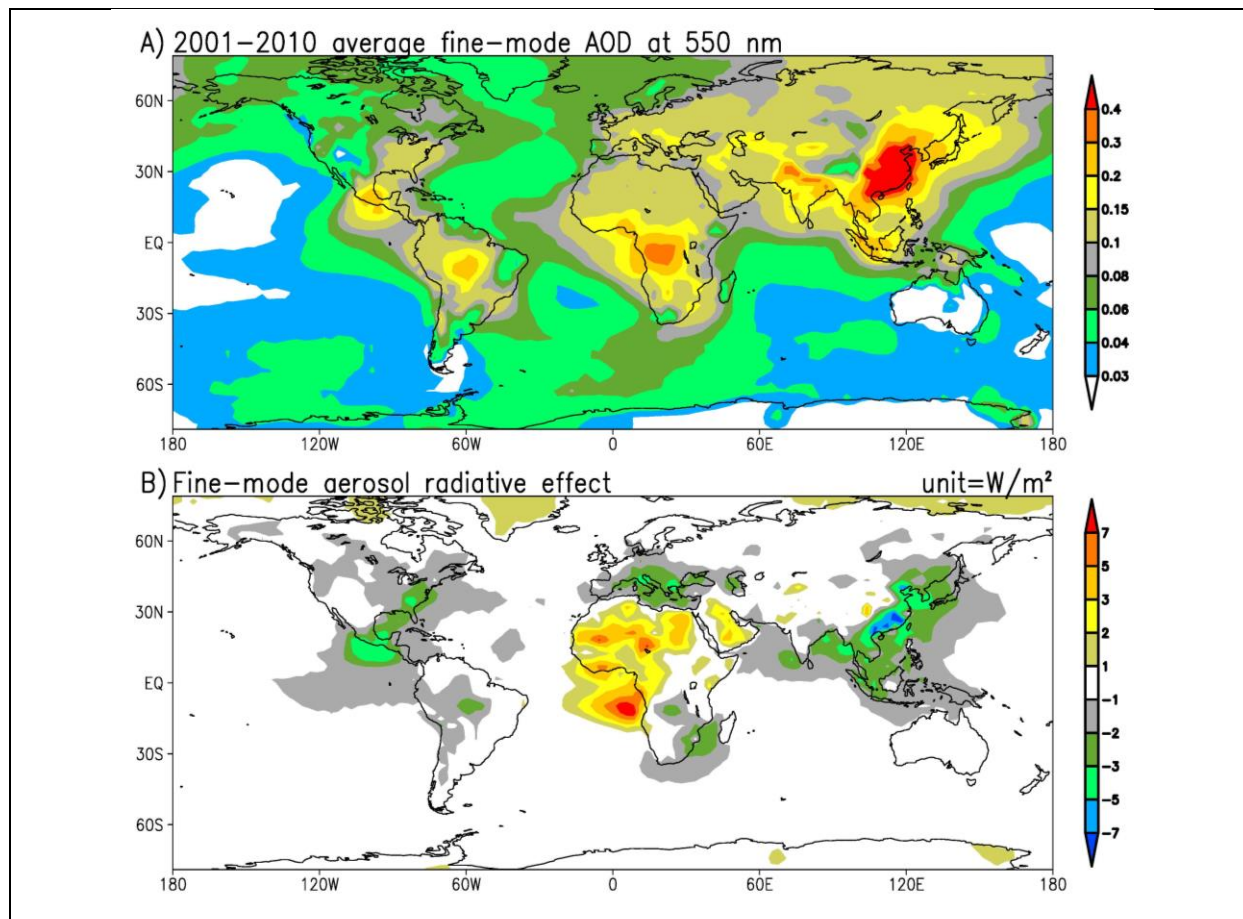


**Figure 3.** A) 2001-2010 mean 550 nm fine-mode AOD (fAOD) obtained by integrating MODIS, MISR, and AERONET data. B) 2001-2010 mean direct fine-mode aerosol radiative effect at TOA in units of  $Wm^{-2}$ ; this estimate includes natural fine-mode particles.

453

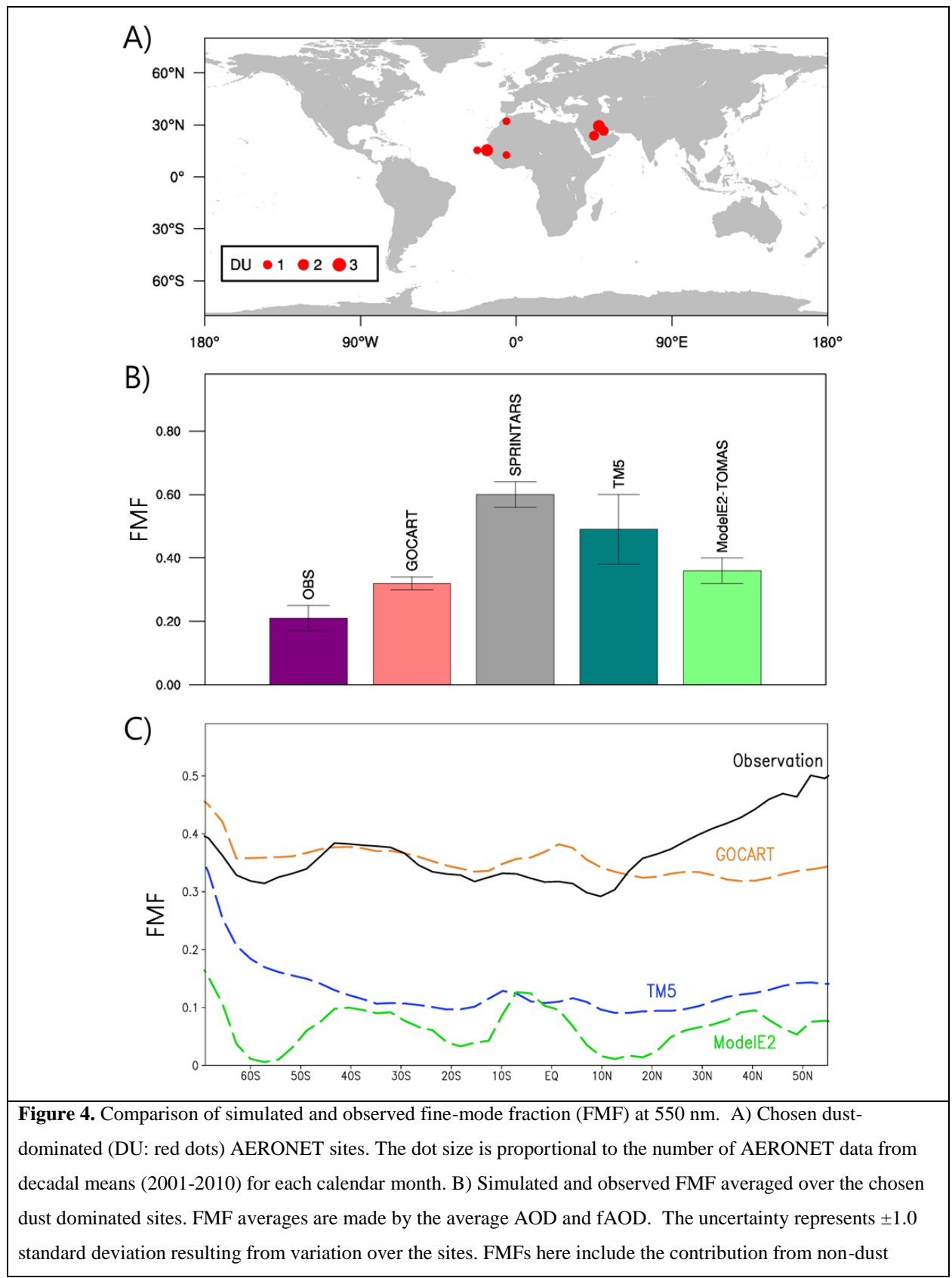


**Figure 4.** Comparison of simulated and observed fine-mode fraction (FMF) at 550 nm. A) Chosen dust-dominated (DU: red dots) AERONET sites. The dot size is proportional to the number of AERONET data from decadal means (2001-2010) for each calendar month. B) Simulated and observed FMF averaged over the chosen dust dominated sites. FMF averages are made by the average AOD and fAOD. The uncertainty represents  $\pm 1.0$  standard deviation resulting from variation over the sites. FMFs here include the contribution from non-dust

particles. C) Sea salt AOD FMF along the 180<sup>th</sup> meridian (180° longitude), using annual average AODs. For observation, total FMF (instead of sea salt AOD FMF) is displayed.

454

455

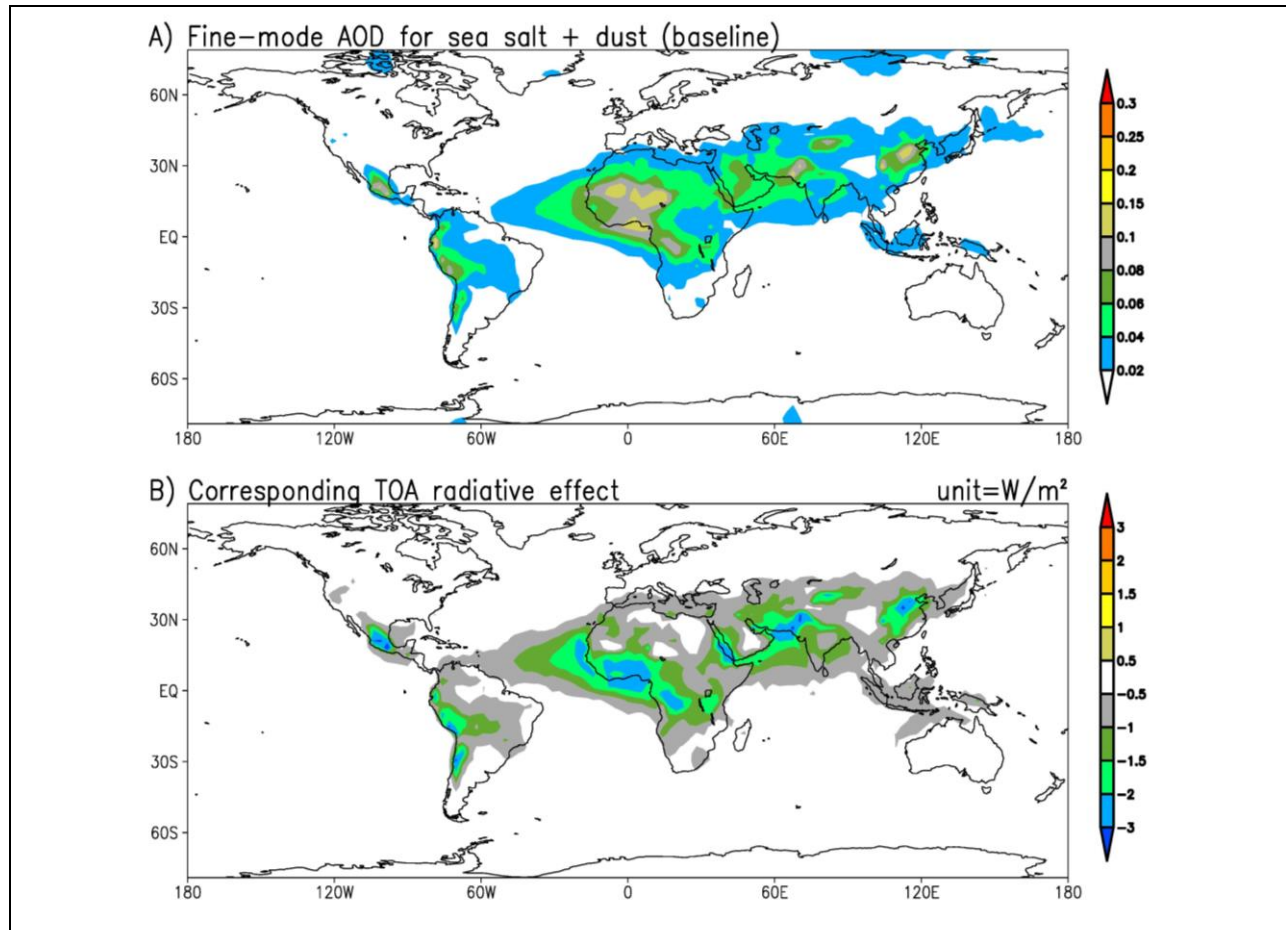


**Figure 5.** A) 2001-2010 mean fine-mode AOD at 550 nm for sea salt and dust, which is calculated as simulated ratio  $\times$  observational large-mode AOD, where the simulated ratio refers to

$$\frac{\text{Model-mix fine-mode AOD for sea salt and dust}}{\text{Model-mix large-mode AOD for sea salt and dust}}$$
 The observational large-mode AOD is computed by integrating AERONET, MODIS and MISR data. Model mix is an optimal mixture of GOCART, TM5 and ModelE2-TOMOS AOD simulations. B) Aerosol direct radiative effect due to the sea salt and dust fine mode aerosols.

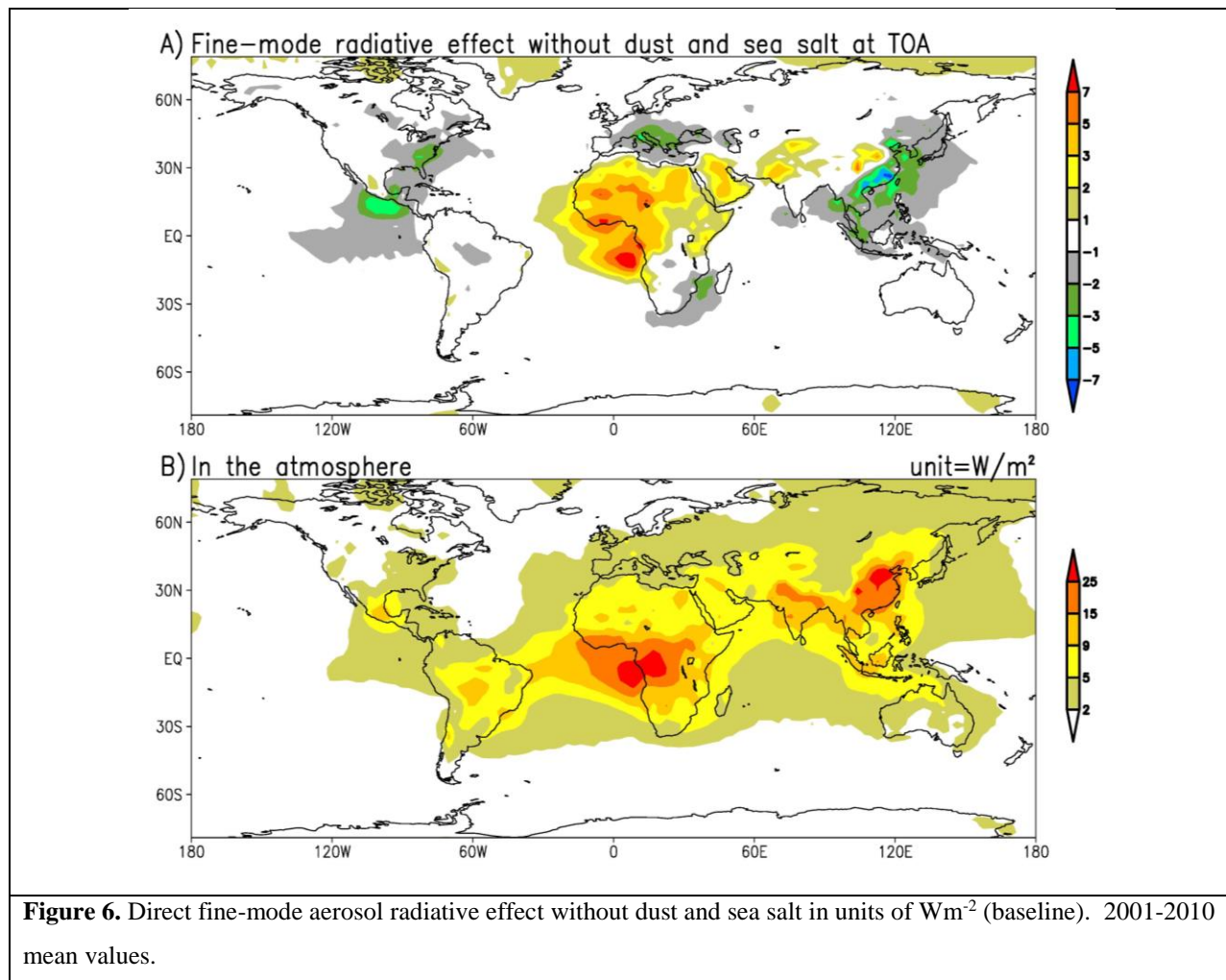


**Figure 6.** Direct fine-mode aerosol radiative effect without dust and sea salt in units of  $Wm^{-2}$  (baseline). 2001-2010 mean values.

458  
 459  
 460  
 461  
 462  
 463  
 464  
 465  
 466